Activity effects on the nonlinear mechanical properties of fire-ant aggregations

Michael Tennenbaum[1,2] and Alberto Fernandez-Nieves[1,2,3]
[1]*School of Physics, Georgia Institute of Technology, Atlanta, Georgia 30332, USA*
[2]*Department of Condensed Matter Physics, University of Barcelona, 08028 Barcelona, Spain*
[3]*ICREA-Instituci Catalana de Recerca i Estudis Avanats, 08010 Barcelona, Spain*

(Received 27 March 2020; accepted 9 June 2020; published 2 July 2020)

Individual fire ants are inherently active as they are living organisms that convert stored chemical energy into motion. However, each individual ant is not equally disposed to motion at any given time. In an active aggregation, most of the constituent ants are active, and vice versa for an inactive aggregation. Here we look at the role activity plays on the nonlinear mechanical behavior of the aggregation through large amplitude oscillatory shear measurements. We find that the level of viscous nonlinearity can be decreased by increasing the activity or by increasing the volume fraction. In contrast, the level of elastic nonlinearity is not affected by either activity or volume fraction. We interpret this in terms of a transient network with equal rates of linking and unlinking but with varying number of linking and unlinking events.

DOI: 10.1103/PhysRevE.102.012602

I. INTRODUCTION

Active matter, in general, is comprised of particles that are each out of equilibrium. All biological systems are active, since living particles constantly convert chemical energy into kinetic energy. Hence, many-particle biological systems, including tissues, flocks of birds, or schools of fish, are all active systems; the principles and theories developed in the active-matter field can then help understand their properties and behavior. Likewise, one can use biological systems to study active matter; this is particularly appealing at high densities, since many biological systems are dense by construction, while much of today's synthetic active matter still remains most applicable under relatively dilute conditions.

Ants, despite their inherent biological complexity, can be thought of as granular-size, active particles. They move and can exist at high densities. Furthermore, they display emergent collective behavior: the properties of ant collectives results from many-body effects, which, albeit in the classical-mechanical realm, are often hard to anticipate based on the behavior and activity of individual ants. While single ants are more likely to be continually active, once there are enough ants together, some become considerably less active while others remain completely inactive [1–3]. The level of activity of single ants in the colony is thus not homogeneous. Furthermore, it is time dependent. Single ants undergo many sleep cycles per day [4], and the ant colony as a whole experiences day and night, seasonal, and short term cycles [5–7]. The spatiotemporal dynamics of ant collectives allow some species to perform large-scale collective motion and build structures [7–9]. Army ants are capable of milling and establish temporary nests and bridges using themselves as the building blocks [10–12].

Fire ants, *Solenopsis invicta*, are also able to link their bodies together in order to form rafts, towers, bridges, and other macroscopic structures [7,13–17]. We refer to fire ant collectives as ant aggregations, as they manifest some degree of cohesiveness; they have, in fact, been compared with cell aggregates with inherent effective attractions between the cells [18]. These ant aggregations move on timescales accessible with rheology and through real-space imaging. They are dense, they percolate through space at densities similar to those inside spontaneously formed rafts, and can be packed to very high numbers. Ant aggregations are thus ideal systems with which to study the role of activity in dense active matter.

We have previously looked at the material properties of fire ant aggregations [19,20]. We saw that at ant-raft densities these aggregations exhibit two distinct behaviors. On the one hand, they can equally be solidlike and liquidlike, with comparable shear elastic and viscous moduli within the frequency-ranged probed in the experiments. On the other hand, they can be predominantly solidlike, with a nearly frequency-independent shear elastic modulus that is significantly larger than the shear viscous modulus. Interestingly, the aggregation switched between these two mechanical responses spontaneously, further affecting the value of the normal force exerted on the upper tool used in the rheology experiments, which we succeeded in relating to the number of active ants in the aggregation. Furthermore, when forced to flow, the aggregation exhibits a shear thinning behavior that compared well with what was observed for dead-ant aggregations, indicating that forcing the aggregation to flow suppresses the role of activity.

In this paper, we extend our studies of ant aggregations into the oscillatory nonlinear regime. We will separate inactive and active behavior by exploiting the spontaneous activity cycles previously observed [20]. We will start by reviewing how to characterize the mechanical nonlinear response, distinguishing between intracycle and intercycle behavior. We will then present results for small amplitude oscillatory shear, where we know that activity plays an important role, and increase the strain amplitude into the nonlinear regime to see if and how activity plays a role in the nonlinear mechanics of the system. Our experiments are some of the first to address the nonlinear mechanical properties of dense active matter.

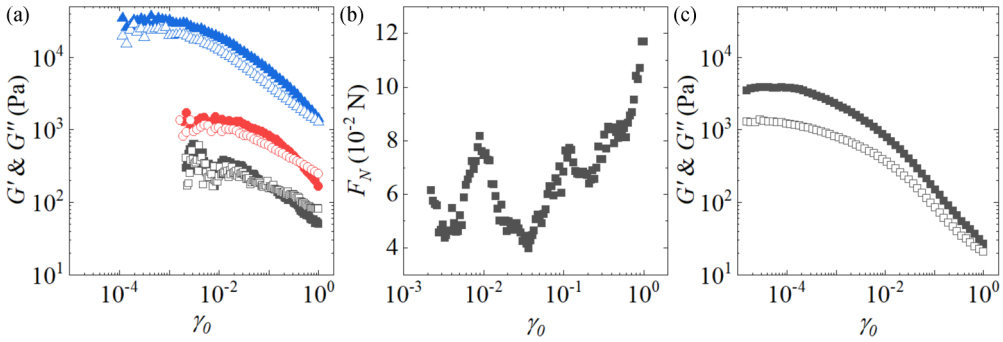

FIG. 1. (a) Strain sweeps for live ants at $\phi_{\text{eff}} = 1.1$ (black squares), 2.2 (red circles), and 3.3 (blue triangles). (b) Normal force data from the strain sweep in (a) at $\phi_{\text{eff}} = 1.1$. (c) Strain sweep for dead ants at $\phi_{\text{eff}} = 1.1$. In (a) and (c), closed symbols represent G', open symbols represent G''. All strain sweeps were performed at $\omega = 1$ rad/s.

II. STRAIN SWEEPS

We start by applying an oscillatory strain, $\gamma(t) = \gamma_0 \sin(\omega t)$, and increasing the strain amplitude γ_0 at fixed frequency ω. This same experiment was discussed in Ref. [19] as a way of finding the linear regime. A similar experiment is shown here in Fig. 1(a), along with a strain amplitude sweep for dead ants, Fig. 1(c). In Fig. 1(a), we show data for different ant densities, which we parametrize using an effective volume fraction, $\phi_{\text{eff}} = \frac{N}{V}(\frac{\pi}{6}l^3)$, where N is the number of ants, V is the accessible volume, which equals the sample volume in our rheology experiments, and l is the average ant length; we find N from the mass of an aggregation and the mean ant mass, which we obtain for each ant colony we use, and find the mean ant length from the corresponding probability distribution. We find that both the storage, G', and loss, G'', moduli are essentially flat up to certain γ_0, above which they decrease with strain amplitude. The noise observed in the constant, linear region at $\phi_{\text{eff}} = 1.1$ mainly results from the proximity to the minimum torque we can meaningfully measure with the rheometer, and from the changing activity of the ants, which is clearly appreciable in the changing normal force in Fig. 1(b) up to $\gamma_0 \leqslant 5 \times 10^{-2}$. Note that the duration of the strain sweep up to that γ_0 is ≈5400 s, which is larger than the time required for the ant aggregation to experience an activity cycle [20]. At even higher strain amplitudes, we find a crossover between the moduli, above which, $G'' > G'$; this is not seen for dead ants, Fig. 1(c). In this regime, the change in the aggregation activity does not seem to affect the mechanical response as much as it does in the linear regime at low γ_0; indeed, note that the second peak in the normal force at $\gamma_0 \approx 10^{-1}$ is much less pronounced than the one at $\gamma_0 \approx 10^{-2}$, indicating that at these large strain amplitudes the system is driven by the applied strain and activity is unable to affect the measurement in any significant manner [20]. The crossover between G' and G'' shifts to higher γ_0 with increasing ϕ_{eff}, see Fig. 1(a), and is often interpreted as a strain-induced fluidization of the system.

However, both the storage and loss moduli only have physical meaning in the linear regime. It is only in this region that they are both to be taken as material properties. Only here are the applied strain and the resultant stress, albeit being out-of-phase, single sinusoids. Beyond the linear regime, both G' and G'' are no longer meaningful, as more than a single sinusoid is, in general, required to describe the measured stress. To understand the behavior outside the linear regime we thus need to go beyond G' and G''. We will use the framework laid out by Ewoldt *et al.* [21], which is based in proposing two viscous and two elastic nonlinear moduli to characterize the nonlinear mechanical properties of materials, emphasizing the distinction between intracycle and intercycle shear moduli; the intercycle moduli allows comparing the moduli at different γ_0, whereas the intracycle moduli provides information about the response within one oscillation at fixed γ_0.

III. LARGE AMPLITUDE OSCILLATORY SHEAR

In large amplitude oscillatory shear (LAOS) an oscillatory strain is applied and the resultant stress is measured. However, unlike in the linear regime where the stress is also sinusoidal, for large amplitude oscillatory strains, the stress is no longer necessarily linear with the applied strain. As such the stress can no longer be represented by a single sinusoid. In Fig. 2(a) we see an example of strain and stress. To decompose the stress into an in-phase component and an out-of-phase component, $\sigma = \sigma' + \sigma''$, we most commonly use a Fourier series.

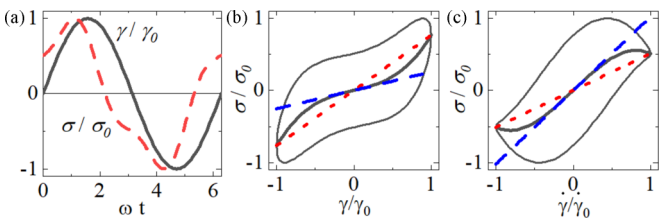

FIG. 2. (a) Waveforms of the strain, $\gamma/\gamma_0 = \sin(\omega t)$ (solid black), and stress $\sigma(t) = (1/\sqrt{2})\sin(\omega t) + (1/\sqrt{2})\cos(\omega t) - (0.2/\sqrt{2})\sin(3\omega t) - (0.2/\sqrt{2})\cos(3\omega t)$ (dashed red), normalized by the maximum stress σ_0, plotted versus dimensionless time, ωt. The level of nonlinearity for this system is $e_3/e_1 = 0.2$ and $v_3/v_1 = -0.2$. (b) The stress σ/σ_0 plotted versus the strain γ/γ_0 for the waveforms in (a). The thick solid black line is σ', the slope of the blue dashed line is G'_M, and the slope of the red dotted line is G'_L. (c) The stress σ/σ_0 plotted versus the shear rate $\dot{\gamma}/\dot{\gamma}_0$ for the waveforms in (a). The thick solid black line is σ'', the slope of the blue dashed line is η'_M, and the slope of the red dotted line is η'_L.

TABLE I. Table for the first Chebyshev functions, T_n, and their recursion relation.

T_0	1
T_1	x
T_2	$2x^2 - 1$
T_3	$4x^3 - 3x$
$T_{n+1}(x)$	$2xT_n(x) - T_{n-1}(x)$

Alternatively, we can represent the stress using Chebyshev functions of the second kind, T_n [21]. Then:

$$\sigma' = \gamma_0 \sum_{n\ \text{odd}} G'_n \sin(n\omega t) = \gamma_0 \sum_{n\ \text{odd}} e_n T_n(x), \tag{1a}$$

$$\sigma'' = \gamma_0 \sum_{n\ \text{odd}} G''_n \cos(n\omega t) = \dot{\gamma}_0 \sum_{n\ \text{odd}} v_n T_n(y), \tag{1b}$$

where $x = \gamma(t)/\gamma_0$ and $y = \dot{\gamma}(t)/\dot{\gamma}_0$. Both the Fourier and Chebyshev series representations produce single valued functions when plotted as a Lissajous curve. We use the x and y normalization because the Chebyshev decomposition is only valid over $[-1, 1]$. The coefficients for the Fourier series are G'_n and G''_n, while the coefficients for the Chebyshev series are e_n and v_n. Hence, in expressions (1a) and (1b), n is the mode number. The first few Chebyshev functions are shown in Table I, though as in the case of the Fourier series, only the odd functions contribute to σ' and σ'' since the applied strain is itself sinusoidal and thus an odd function of time.

The practicality of the Chebyshev series is most easily seen when plotting the stress versus the strain or the shear rate in a Lissajous form, see Figs. 2(b), 2(c). Here we have normalized the stress by the maximum stress σ_0. In these figures, we also plot, using solid black lines, the elastic (σ') and viscous (σ'') components, respectively. Since $T_1(x) = x$, any deviation from linear behavior in the stress, where these lines would be straight lines, is immediately captured by the coefficients for $T_3(x)$, which are either e_3 or v_3. A positive e_3 describes an increase in stress above linear at the highest strains; this is in-cycle, or intracycle, strain stiffening, see Fig. 2(b). In-cycle, or intracycle, strain softening corresponds to negative e_3 and a stress that is lowered at the highest strain. Similarly, when v_3 is positive, there is intracycle shear thickening, corresponding to a stress that increases at high shear rate, and when v_3 is negative, there is intracycle shear thinning, corresponding to a stress that decreases at high shear rate; this last behavior is illustrated in Fig. 2(c).

In the linear regime $e_1 = G'$ and $v_1 = G''/\omega$. However, outside the linear regime, there is not a single slope for the in-phase component or the out-of-phase component of the stress, and thus there is no longer a single elastic modulus or a single viscous modulus. Ewoldt *et al.* defined four nonlinear moduli, two each for the elastic and viscous components [21]. The two elastic moduli are the minimum strain elastic modulus, G'_M, and the large strain elastic modulus, G'_L. The modulus G'_M is the slope of the in-phase stress when the strain is zero. It can be found from either the Fourier or Chebyshev coefficients:

$$G'_M = \left.\frac{d\sigma'}{d\gamma}\right|_{\gamma=0} = \sum_{n\ \text{odd}} nG'_n = \sum_{\text{n odd}} ne_n(-1)^{(n-1)/2}. \tag{2}$$

The modulus G'_L is the slope of the line connecting the stress at the minimum strain to the stress at the maximum strain:

$$G'_L = \frac{\sigma'(\gamma = \gamma_0) - \sigma'(\gamma = -\gamma_0)}{2\,\gamma_0} = \sum_{n\ \text{odd}} G'_n(-1)^{(n-1)/2}$$

$$= \sum_{\text{n odd}} e_n. \tag{3}$$

Both G'_M and G'_L are represented by the dashed and dotted lines, respectively, in Fig. 2(b).

The two viscous moduli are defined in a similar way from σ'' and the shear rate, with a minimum shear rate viscous modulus, η'_M, and a large shear rate viscous modulus, η'_L:

$$\eta'_M = \left.\frac{d\sigma''}{d\dot{\gamma}}\right|_{\dot{\gamma}=0} = \frac{1}{\omega}\sum_{n\ \text{odd}} nG''_n = \sum_{n\ \text{odd}} nv_n(-1)^{(n-1)/2}, \tag{4}$$

$$\eta'_L = \frac{\sigma''(\dot{\gamma} = \dot{\gamma}_0) - \sigma''(\dot{\gamma} = -\dot{\gamma}_0)}{2\,\dot{\gamma}_0} = \frac{1}{\omega}\sum_{n\ \text{odd}} G''_n(-1)^{(n-1)/2}$$

$$= \sum_{n\ \text{odd}} v_n. \tag{5}$$

Both η'_M and η'_L are represented by the dashed and dotted lines, respectively, in Fig. 2(c).

We also define the level of nonlinearity by comparing G'_M to G'_L and η'_M to η'_L. In the linear regime, $G'_M = G'_L = G'$ and $\eta'_M = \eta'_L = G''/\omega$. Outside of the linear regime, if $G'_L > G'_M$, the stress has increased above linear at large strains and so there is intracycle strain stiffening. Intracycle strain softening corresponds to $G'_L < G'_M$. The level of elastic nonlinearity, S, is defined as:

$$S = \frac{G'_L - G'_M}{G'_L} = \frac{4e_3 + \ldots}{e_1 + e_3 + \ldots} \sim \frac{e_3}{e_1}. \tag{6}$$

It is zero in the linear regime, and positive or negative for intracycle strain stiffening or strain softening materials, respectively. If we expand the moduli in terms of the Chebyshev coefficients, we can see that S is essentially determined by e_3/e_1, since e_3 is always less than e_1. The sign of e_3 then directly determines whether the material intracycle strain stiffens or strain softens.

For the viscous moduli, $\eta'_L > \eta'_M$ implies intracycle shear thickening, since at large shear rates the stress is higher than linear, and $\eta'_L < \eta'_M$ implies intracycle shear thinning. The level of viscous nonlinearity is: $T = (\eta'_L - \eta'_M)/\eta'_L$. It is zero in the linear regime, positive for intracycle shear thickening materials, and negative for intracycle shear thinning materials. It is also proportional to v_3/v_1, given that $v_3 \ll v_1$. We then see that the level of nonlinearity as well as the type is characterized by e_3/e_1 and v_3/v_1, to leading order, since e_1 and v_1 are always positive. Either S and T or e_3/e_1 and v_3/v_1 can be used to quantify the level of nonlinearity in a system.

Another interesting feature of the nonlinear moduli is that the moduli are not required to be positive. If this happens, it is more likely to happen in the minimum strain moduli, since $G'_M \sim e_1 - 3e_3$ whereas $G'_L \sim e_1 + e_3$. The same is true for the minimum shear rate moduli. For example, G'_M would be negative when the slope of the in-phase stress is negative around $\gamma = 0$. This would also appear as a self-intersection in the out-of-phase Lissajous curve at high shear rate. A negative

modulus indicates that the material is unloading stress faster than it is accumulating it. This is a long-time effect and would not appear on the first oscillation since it is impossible to unload stress that has not been loaded yet.

We find the coefficients in the series expansion by fitting a sum of sines to the waveforms or fitting to Chebyshev functions. In practice, this is done by taking a fast Fourier transform (FFT) of the stress waveform, which gives the weights of the sine fit and then calculating the Chebyshev coefficients. Fast Fourier transforms are a class of algorithms that compute the Fourier transform of a discrete set of points n, using a number of points of order $O(n \log n)$, which are significantly less than the $O(n^2)$ points required when computing the Fourier transform directly. The rheometer records 257 points for each waveform, with the last point overlapping with the first. This means that there are 256 points in a full cycle, with constant time step. The number of points is also a power of 2, which is convenient but not required for the FFT algorithm. This also sets the maximum number of Fourier or Chebyshev modes that we can use to 128, as the Nyquist frequency $\omega_{\text{Nyquist}} = N_p/2$ [21], with $N_p = 256$ the number of sampling points. In practice, however, we never need this many. First, since we only care about odd modes because the stress is assumed to be odd [21,22], and second because the first few modes contribute the most to the shape; the majority of experiments are captured using the first two odd modes. We use the first 11 odd modes out of a possible 64 modes to determine the nonlinear moduli and to calculate the Chebyshev coefficients.

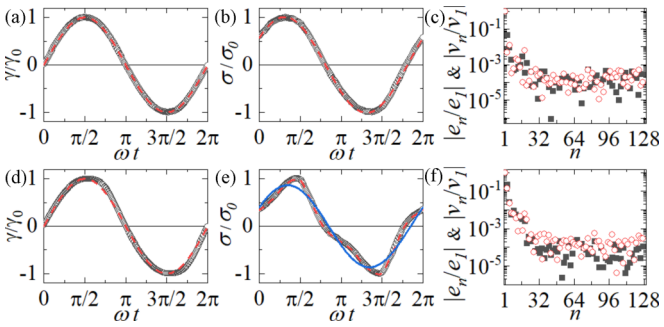

FIG. 3. (a)–(c) Oscillatory measurement in the linear regime for a live aggregation at $\phi_{\text{eff}} = 1.6$, $\omega = 10$ rad/s, and $\gamma_0 = 0.01$. (a) Normalized strain vs phase angle. The dashed line is a fit to $\gamma = \gamma_0 \sin(\omega t)$. (b) Normalized stress vs phase angle for the same measurement. The dashed line is a reconstruction from the first Chebyshev coefficient. (c) The magnitude of the Chebyshev coefficients normalized with the first coefficient. (d)–(f) Oscillatory measurement outside the linear regime for a live aggregation at $\phi_{\text{eff}} = 1.6$, $\omega = 10$ rad/s, and $\gamma_0 = 1$. (d) Normalized strain vs phase angle. The dashed line is a fit to $\gamma = \gamma_0 \sin(\omega t)$. The deviation at high strain does not affect the calculation of nonlinear moduli since only the magnitude of γ_0 is used. It does, however, affect how the viscous Lissajous curve looks. (e) Normalized stress vs phase angle for the same measurement. The line is a reconstruction from the first (solid blue) and the first 11 (dashed red) coefficients. (f) The magnitude of the Chebyshev coefficients normalized with the first coefficient. (c), (f) The closed black squares are the elastic coefficients, e_n/e_1, and the open red circles are the viscous coefficients, v_n/v_1.

IV. ANT LISSAJOUS RECONSTRUCTIONS

We illustrate this reconstruction for an ant aggregation at $\phi_{\text{eff}} = 1.6$ for two representative strain amplitudes: $\gamma_0 = 0.01$ and $\gamma_0 = 1$. Their waveforms and reconstructions are shown in Figs. 3(a), 3(b) and 3(d), 3(e). The absolute value of the relative contributions of each mode number for the stress waveforms are shown in Figs. 3(c) and 3(f). The relative weight is found by normalizing with respect to the first mode; we plot the absolute values, since the contributions can be negative, and use a semilog scale to emphasize the importance of only the first few modes. From the coefficients we can then calculate the nonlinear moduli as well as the in-phase and out-of-phase stress components, σ' and σ''. The moduli and the stress components are shown in Fig. 4, overlaid over the Lissajous curves for the example waveforms in Figs. 3(a), 3(b) and 3(d), 3(e).

We see good agreement between the strain and stress and reconstructions using only the first mode in the linear regime, Figs. 3(a), 3(b) and 4(a), 4(b). However, only using a single mode certainly does not fit the stress response outside of the linear regime, Fig. 3(e). Considering the first 11 modes gives a good fit of the stress.

Looking at the Lissajous curves both in the linear and nonlinear regimes gives us several criteria for determining if a point is reasonable and removing outliers from the data set. This allows us to use points that are really close to or at the torque limit of the rheometer and to neglect points that are below the torque limit automatically. From the shape we can determine that the moduli are not negative for ant aggregations. Hence, points in our analysis that have negative moduli are automatically neglected. We also neglect data with a level of nonlinearity that significantly differs from the average. If $|(S/4 - e_3/e_1)| > 1$ or $|(T/4 - v_3/v_1)| > 1$ we remove the point.

Using Eq. (6), we can rewrite these inequalities in terms of e_3/e_1 or v_3/v_1. In the first case,

$$\left|\frac{S}{4} - \frac{e_3}{e_1}\right| = \left|\frac{e_3 + \ldots}{e_1 + e_3 + \ldots} - \frac{e_3}{e_1}\right| \approx \left|\frac{(e_3/e_1)^2}{1 + (e_3/e_1)}\right| > 1. \quad (7)$$

An equivalent expression can be written in terms of v_3/v_1. We will then neglect points whenever e_3/e_1 and v_3/v_1 lie outside of $\pm(1 + \sqrt{5})/2 \approx \pm 1.6$. This is a reasonable range since at the highest strain amplitude we have explored, $\gamma_0 = 1$, $e_3/e_1 \approx 0.2$, and $v_3/v_1 \approx -0.25$. For example, the data in Figs. 4(c) and 4(d) is at $\gamma_0 = 1$, and has $e_3/e_1 = 0.22$ and $v_3/v_1 = -0.15$.

Before moving on to the next section, we would like to comment on the slight deviation in the strain at high strain amplitude directly after the system has reached the largest strain, see Fig. 3(d). This is likely due to the nonzero feedback loop of our stress-controlled rheometer, which is operated in oscillatory rheology in a strain-controlled mode. Nevertheless, the observed deviation does not affect the elastic nonlinear moduli, since the reconstruction is good at the minimum and the maximum strains, see Fig. 4(c). It does affect, however, the viscous nonlinear moduli by overestimating η_L' and underestimating η_M', see Fig. 4(d). This means that at the highest strain amplitudes the value of v_3/v_1 or T is in reality smaller in

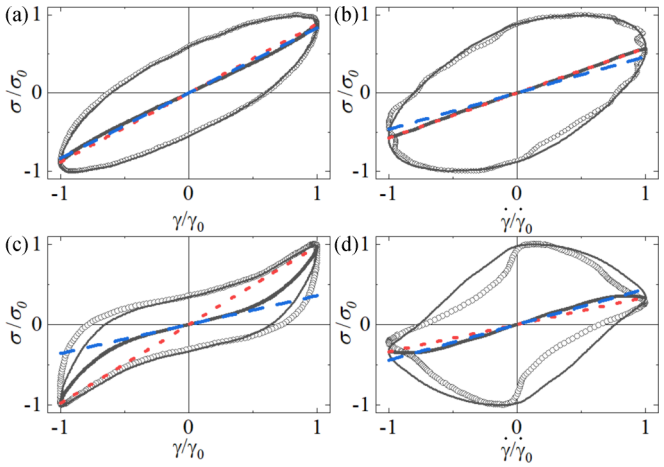

FIG. 4. (a)–(b) Lissajous curves for an oscillatory measurement in the linear regime for a live aggregation at $\phi_{\text{eff}} = 1.6$, $\omega = 10$ rad/s, and $\gamma_0 = 0.01$. The waveforms are shown in Figs. 3(a), 3(b). (a) Elastic Lissajous curve (black circles) and reconstruction (thin black line). σ' (thick black line), the line with slope G'_L (red dotted line), and the line with slope G'_M (blue dashed line) are all overlapping lines. (b) Viscous Lissajous curve (black circles) and reconstruction (thin black line). σ'' (thick black line), the line with slope η'_L (red dotted line), and the line with slope η'_M (blue dashed line) are all overlapping lines. (c)–(d) Lissajous curves for an oscillatory measurement outside the linear regime for a live aggregation at $\phi_{\text{eff}} = 1.6$, $\omega = 10$ rad/s, and $\gamma_0 = 1$. The waveforms are shown in Figs. 3(d), 3(e). (c) Elastic Lissajous curve (black circles) and reconstruction (thin black line). σ' is the thick black line, G'_L is the slope of the red dotted line, and G'_M is the slope of the blue dashed line. (d) Viscous Lissajous curve (black circles) and reconstruction (thin black line). σ'' is the thick black line, η'_L is the slope of the red dotted line, and η'_M is the slope of the blue dashed line. The deviations in the strain seen in Fig. 3(d) show up in the elastic Lissajous curve and are pronounced in the viscous Lissajous curve.

magnitude than what we find from our fits. The placement of the deviation means that the deviations in strain rate are at the minimum and maximum values while the deviations in strain are between the minimum and maximum, thereby causing a larger effect on T than on S.

A. Binning by activity

We also want to be able to look at the effect the level of activity has on the level of nonlinearity and the nonlinear moduli. We have seen in previous work that activity affects the mechanics of ant aggregations [20]. There we saw that we could determine the level of activity by looking at the normal force that the aggregation exerts on the top tool. This was clearly seen in creep experiments and linear oscillatory rheology, both of which showed cyclic peaks in the normal force. An example of such behavior is shown in Fig. 5. Overlaid on the peaks in the normal force are the cutoffs we use to classify each measurement as either inactive, active, or transitional. Active points have high normal force and capture the peaks of activity. Inactive points have low normal force and capture the instance of an aggregation when it is predominantly static and inactive. The middle, transitional section has intermediate

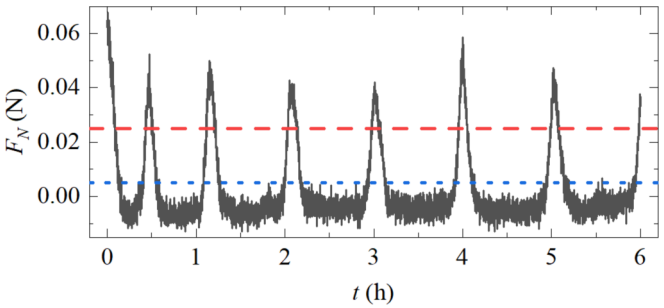

FIG. 5. Normal force as a function of time illustrating the cyclic changes of the level of activity. The lower blue dotted line is the upper cutoff limit of what we are classifying as inactive. The upper red dashed line is the lower cutoff limit of what we are classifying as active.

normal force and displays properties between what we have called active and inactive. We will be comparing the active to the inactive case and using the transitional measurements as a buffer to separate the two.

Since we need to do long time measurements to obtain data when the aggregation is active and inactive we will focus on just a few points all at $\omega = 1$ rad/s. This frequency was chosen to have high enough torque to be able to measure at all γ_0 while avoiding noise at higher frequencies. We use different colonies with different captivity times and bin the data in terms of active or inactive to construct probability distributions for all properties of interest; the number of data points used to obtain these distributions is indicated in Table II.

V. INTRACYCLE RESULTS

At the largest strain amplitude, $\gamma_0 = 1$, the aggregation is far from the linear regime. The level of elastic nonlinearity is around 0.2 and is unaffected by the level of activity, Fig. 6(a). Positive e_3/e_1 indicates intracycle strain stiffening corresponding to the increase in stress at high strain in the Lissajous curve in Fig. 4(c). The elastic modulus G'_L is larger than G'_M and neither is affected by the level of activity, Figs. 6(b), 6(c). The level of viscous nonlinearity is around -0.25 and is unaffected by activity, Fig. 6(d). It is negative indicating intracycle shear thinning, consistent with the Lissajous curve in Fig. 4(d). The viscous modulus η'_M is larger than η'_L and neither is affected by the level of activity, Figs. 6(e), 6(f). We thus conclude that at strain amplitudes this high, the forcing effect of the large strain is enough to wash out the effects of

TABLE II. The number of active and inactive points measured at each effective volume fraction and strain amplitude.

		$\gamma_0 = 0.01$	$\gamma_0 = 0.1$	$\gamma_0 = 1$
$\phi_{\text{eff}} = 1.1$	Active	620	308	2490
	Inactive	703	366	800
$\phi_{\text{eff}} = 1.6$	Active	997	1368	756
	Inactive	663	1083	341

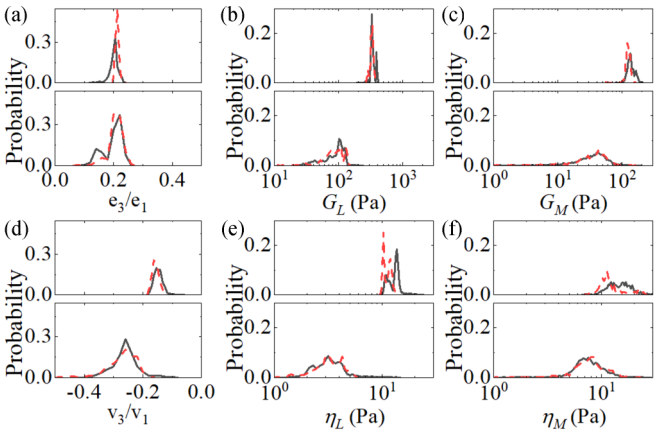

FIG. 6. (a)–(f) Probability distributions for the level of nonlinearity and the nonlinear moduli for a strain amplitude $\gamma_0 = 1$. Bottom panels are at $\phi_{\text{eff}} = 1.1$ and top panels are at $\phi_{\text{eff}} = 1.6$. Solid black lines are for active aggregations, and red dashed lines are for inactive aggregations. Elastic properties are shown in (a)–(c) in terms of (a) e_3/e_1, (b) G'_L, and (c) G'_M. Viscous properties are shown in (d)–(f) in terms of (d) v_3/v_1, (e) η'_L, and (f) η'_M. All distributions have been normalized by the number of points in the distribution, see Table II.

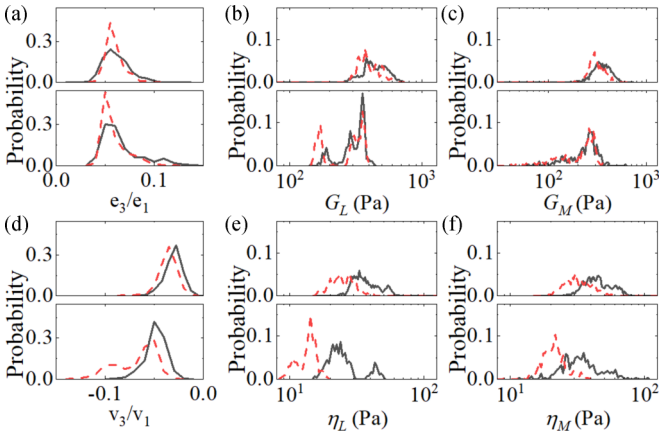

FIG. 7. (a)–(f) Probability distributions for the level of nonlinearity and the nonlinear moduli for a strain amplitude $\gamma_0 = 0.1$. Lower panels are at $\phi_{\text{eff}} = 1.1$ and upper panels are at $\phi_{\text{eff}} = 1.6$. Solid black lines are for active aggregations, and dashed red lines are for inactive aggregations. Elastic properties are shown in (a-c) in terms of (a) e_3/e_1, (b) G'_L, and (c) G'_M. Viscous properties are shown in (d)–(f) in terms of (d) v_3/v_1, (e) η'_L, and (f) η'_M. All distributions have been normalized by the number of points in the distribution, see Table II.

activity from the behavior of the system. This is reminiscent of how dead and live ants flow the same way when forced to flow during a controlled shear rate experiment [19].

At $\gamma_0 = 0.1$ the aggregation intracycle strain stiffens, as indicated by the positive value of e_3/e_1, Fig. 7(a) lower panel. The level of nonlinearity does not change with activity, and G'_L is larger than G'_M; neither of them change with activity, Figs. 7(b), 7(c) lower panels. Similarly to the results obtained at $\gamma_0 = 1$, the level of viscous nonlinearity is always negative. However, in this case, it does change with activity. Increasing activity decreases the level of viscous nonlinearity from -0.06 ± 0.02 to -0.04 ± 0.01, Fig. 7(d) lower panel. Activity increases both nonlinear viscous moduli, but it increases the large strain rate modulus by a larger amount thereby decreasing the level of nonlinearity, Figs. 7(e), 7(f) lower panels.

We can think of the change in the level of viscous nonlinearity and the lack of change in the level of elastic nonlinearity in terms of the ant network, and in particular the connections between the ants. Vernerey *et al.* proposed that in a transient network the mechanics would be dependent on the rate of attachment and detachment in the system [23–25]. From the elastic behavior, we see that on average the network is unchanged by activity. In terms of linking and unlinking events this means that the rate of linking and unlinking must be similar. The specific links change but, on average, the network is not different; the number of connections remains unchanged on average.

To understand the change with activity of the level of viscous nonlinearity, we consider that in the active case, the number of linking and unlinking events is larger than in the inactive case. This causes the level of viscous nonlinearity to decrease, or in other words, it causes the system to behave in the active case in a way that is closer to the linear regime.

To test this interpretation of the results, we change the ant density. The rationale behind this is that increasing ϕ_{eff} should increase the number of linking and unlinking events, and hence decrease the level of viscous nonlinearity. The level of elastic nonlinearity, however, should remain essentially unchanged, since the ratio of linking to unlinking events should be the same.

Let us first consider experiments at $\gamma_0 = 1$. Indeed, we find that increasing ϕ_{eff} does not change the level of elastic nonlinearity, see Fig. 6(a) upper panel. In contrast, the elastic nonlinear moduli increase, see upper panels in Figs. 6(b) and 6(c), as expected, given that on average the number of connections increases with ϕ_{eff}. Again, neither the moduli or e_3/e_1 are affected by activity. The viscous moduli also increase in value and also remain unaffected by activity, see upper panels in Figs. 6(e) and 6(f). The level of viscous nonlinearity, however, decreases with increasing ϕ_{eff}, see Fig. 6(d), indicating that the number of linking and unlinking events has indeed increased with the increased density.

Similarly, at $\gamma_0 = 0.1$, increasing ϕ_{eff} do not change the level of elastic nonlinearity. In contrast, the moduli does increase, see Figs. 7(a)–7(c) upper panels. Again, activity has no effect, indicating that the network structure is unchanged on average. For the viscous component, however, increasing ϕ_{eff} decreases the level of nonlinearity and causes the moduli to increase, Figs. 7(e)–7(f) upper panels.

Our results thus confirms that increasing the number of linking and unlinking events decreases v_3/v_1 and that this can be achieved either through increasing the ant density or by increasing the activity. Though increasing the activity has a smaller effect than changing ϕ_{eff}, either can be used as a tuning parameter to change the dissipation in the system.

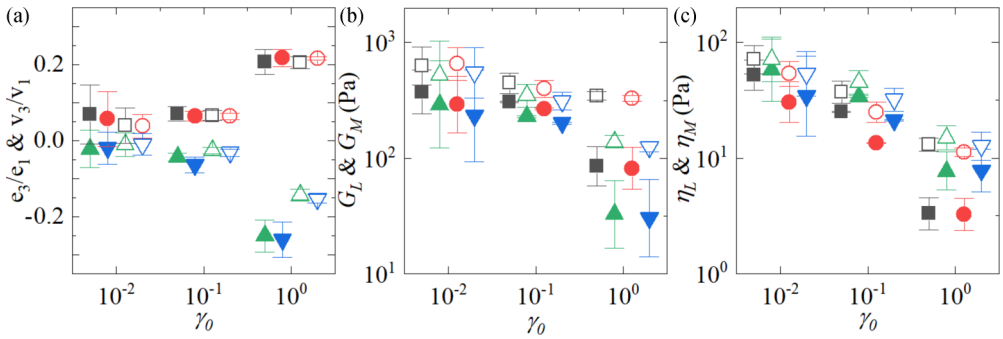

FIG. 8. Nonlinear moduli and the level of nonlinearity for ant aggregations at $\phi_{\text{eff}} = 1.1$ (closed symbols) and $\phi_{\text{eff}} = 1.6$ (open symbols). (a) e_3/e_1 for active ants (black squares), e_3/e_1 for inactive ants (red circles), v_3/v_1 for active ants (green up triangles), v_3/v_1 for inactive ants (blue down triangles). (b) G'_L for active ants (black squares), G'_L for inactive ants (red circles), G'_M for active ants (green up triangles), G'_M for inactive ants (blue down triangles). (c) η'_L for active ants (black squares), η'_L for inactive ants (red circles), η'_M for active ants (green up triangles), η'_M for inactive ants (blue down triangles).

VI. INTERCYCLE EFFECTS OF STRAIN AMPLITUDE AND EFFECTIVE VOLUME FRACTION

We can now combine data for different γ_0 to address what is happening intercycle when changing the applied strain amplitude and the effective volume fraction. At low strain amplitudes, $\gamma_0 \approx 10^{-2}$, the levels of both elastic and viscous nonlinearity are around zero though the mean elastic nonlinearity is slightly positive and the mean viscous nonlinearity is slightly negative, Fig. 8(a). Lower values of γ_0 seem to be needed to be in the strict linear regime; these are, however, not accessible due to the low torque of the samples in such conditions. As γ_0 increases, the standard deviation of the elastic nonlinearity distribution considerably decreases, indicating that at these strain amplitudes the elastic nonlinearity is always positive. Similarly, the standard deviation of the viscous nonlinearity distribution also considerably decreases; the viscous nonlinearity is thus always negative. Increasing activity slightly decreases the level of nonlinearity.

At $\gamma_0 \approx 1$ the aggregation intracycle strain stiffens, as seen from the positive e_3/e_1 values, and intracycle shear thins, seen from the negative v_3/v_1 values, Fig. 8(a). Activity does not play a significant role.

Increasing ϕ_{eff} does not change the level of elastic nonlinearity at any strain amplitude. The viscous nonlinearity decreases with increasing ϕ_{eff} and this change is larger for larger γ_0, Fig. 8(a). There is a change in the viscous nonlinearity with activity at $\gamma_0 \approx 0.1$ but the effect is small compared to ϕ_{eff}.

While the system intracycle shear thins and strain stiffens we can now also look at the intercycle behavior. Ant aggregations intercycle strain soften, which is seen from the decreasing magnitude of the elastic moduli in Fig. 8(b). They intercycle shear thin, as seen from the decreasing magnitude of the viscous moduli, Fig. 8(c), and consistent with controlled shear experiment [19].

Our results for the nonlinear shear moduli are consistent with the strain amplitude sweeps shown in Fig. 1, and the storage and loss moduli obtained there by assuming a linear response. This is likely due to not having reached a strongly nonlinear regime in our experiments. If we had, not even qualitative information could be extracted from the values of G' and G''. The description in terms of G'_L, G'_M, η'_L, and η'_M is thus not only correct, but required in the nonlinear regime to, at the very least, assess whether an even qualitative interpretation of G' and G'' is possible.

VII. CONCLUSIONS

Ant aggregations intercycle strain soften and shear thin with increasing strain amplitude. Within one cycle however, at higher strain amplitudes, they strain stiffen and shear thin.

The level of elastic nonlinearity shows intracycle strain stiffening irrespective of activity or effective volume fraction. The nonlinear moduli, however, are affected by ϕ_{eff}; they increase with effective volume fraction, consistent with having a larger number density of ants and thus with having a larger number of ant connections per unit volume. The level of elastic nonlinearity is based on the overall structure of the network, which does not seem to change likely due to the rates of linking and unlinking events between ants being comparable. Neither activity nor effective volume fraction within the range probed in our experiments affects the level of elastic nonlinearity.

The level of viscous nonlinearity shows intracycle shear thinning and is affected by both the activity and the effective volume fraction. It decreases with increasing activity or increasing effective volume fraction. The dissipation rate and hence the viscous nature of the aggregation is affected by the number of linking and unlinking events that take place inside the system. This increases with activity and with effective volume fraction, which results in a lower level of viscous nonlinearity.

Overall, our results show that the nonlinear mechanics of the system can be tuned with activity. On average the structure itself is not changing, as reflected by the constant level of elastic nonlinearity, but the dissipation does change with activity. In real life, having elastic properties unaffected by activity could prove useful in maintaining the integrity of ant rafts and towers [15]. In contrast, having internal dynamics, which dissipate energy, results in restructuring and distribution of loads between ants; this results in no single ant having to remain for long times at a given location within the structure subjected to, for example, the weight of the ants on top of it.

Overall, our results indicate that two systems with the same average structure can exhibit different mechanical properties as a result of ant density and activity.

ACKNOWLEDGMENT

We thank MCIU/AEI/FEDER, UE (Grant No. PGC2018-336 097842-B-I00).

[1] M. Vela-Perez, M. A. Fontelos, and S. Garnier, Math. Biosci. **262**, 56 (2015).
[2] J. Aguilar, D. Monaenkova, V. Linevich, W. Savoie, B. Dutta, H.-S. Kuan, M. Betterton, M. Goodisman, and D. Goldman, Science **361**, 672 (2018).
[3] J. Chen, *Insect Science* (Wiley, New York, 2020).
[4] D. L. Cassill, S. Brown, D. Swick, and G. Yanev, J. Ins. Behav. **22**, 313 (2009).
[5] B. J. Cole, Am. Nature **137**, 244 (1991).
[6] W. R. Tschinkel, Ecological Monographs **63**, 425 (1993).
[7] W. R. Tschinkel, *The Fire Ants* (Harvard University Press, Cambridge, 2006).
[8] B. Holldobler, *The Ants* (Harvard University Press, Cambridge, 1990).
[9] T. C. Schneirla, *Army Ants: A Study in Social Organization* (W. H. Freeman, New York, 1971).
[10] T. C. Schneirla, *A Unique Case of Circular Milling in Ants, Considered in Relation to Trail Following and the General Problem of Orientation* (American Museum of Natural History, New York, 1944).
[11] I. D. Couzin and N. R. Franks, Proc. Biol. Sci. **270**, 139 (2003).
[12] C. R. Reid, M. J. Lutz, S. Powell, A. B. Kao, I. D. Couzin, and S. Garnier, Proc. Natl. Acad. Sci. USA **112**, 15113 (2015).
[13] N. J. Mlot, C. A. Tovey, and D. L. Hu, Proc. Natl. Acad. Sci. USA **108**, 7669 (2011).
[14] N. J. Mlot, C. Tovey, and D. L. Hu, Commun. Integr. Biol. **5**, 590 (2012).
[15] P. C. Foster, N. J. Mlot, A. Lin, and D. L. Hu, J. Exp. Biol. **217**, 2089 (2014).
[16] D. L. Cassill, A. Casella, J. Clayborn, M. Perry, and M. Lagarde, J. Bioecon. **17**, 255 (2015).
[17] S. Phonekeo, N. Mlot, D. Monaenkova, D. L. Hu, and C. Tovey, Roy. Soc. Open Sci. **4**, 170475 (2017).
[18] D. Hu, S. Phonekeo, E. Altshuler, and F. Brochard-Wyart, Eur. Phys. J.: Spec. Top. **225**, 629 (2016).
[19] M. Tennenbaum, Z. Liu, D. Hu, and A. Fernandez-Nieves, Nature Mater. **15**, 54 (2016).
[20] M. Tennenbaum and A. Fernandez-Nieves, Phys. Rev. E **96**, 052601 (2017).
[21] R. H. Ewoldt, A. Hosoi, and G. H. McKinley, J. Rheol. (1978–present) **52**, 1427 (2008).
[22] R. B. Bird, R. C. Armstrong, and O. Hassager, *Dynamics of Polymeric Liquids. Vol. 1: Fluid Mechanics* (Wiley, New York, 1987).
[23] F. J. Vernerey, R. Long, and R. Brighenti, J. Mech. Phys. Solids **107**, 1 (2017).
[24] F. J. Vernerey, T. Shen, S. L. Sridhar, and R. J. Wagner, J. R. Soc., Interface **15**, 20180642 (2018).
[25] F. J. Vernerey, E. Benet, L. Blue, A. K. Fajrial, S. Lalitha Sridhar, J. S. Lum, G. Shakya, K. H. Song, A. N. Thomas, and M. A. Borden, Adv. Colloid Interface Sci. **263**, 38 (2019).